

# PhysSFI-Net: Physics-informed Geometric Learning of Skeletal and Facial Interactions for Orthognathic Surgical Outcome Prediction

Jiahao Bao<sup>1#</sup>, Huazhen Liu<sup>2#</sup>, Yu Zhuang<sup>3#</sup>, Leran Tao<sup>4</sup>, Xinyu Xu<sup>5</sup>, Yongtao Shi<sup>6</sup>, Mengjia Cheng<sup>7</sup>, Yiming Wang<sup>8</sup>, Congshuang Ku<sup>9</sup>, Ting Zeng<sup>10</sup>, Yilang Du<sup>11</sup>, Siyi Chen<sup>12</sup>, Shunyao Shen<sup>13\*</sup>, Suncheng Xiang<sup>14\*</sup>, Hongbo Yu<sup>15\*</sup>

## Affiliation:

1 Department of Oral and Craniomaxillofacial Surgery, Shanghai Ninth People's Hospital, Shanghai Jiao Tong University School of Medicine; College of Stomatology, Shanghai Jiao Tong University; National Center for Stomatology; National Clinical Research Center for Oral Diseases, Shanghai Key Laboratory of Stomatology; Shanghai Research Institute of Stomatology, Shanghai, 200011, China. E-mail: [baojh0123@sjtu.edu.cn](mailto:baojh0123@sjtu.edu.cn)

2 School of Electronic Information and Electrical Engineering, Shanghai Jiao Tong University, Shanghai, China. E-mail: [huazhenliu@sjtu.edu.cn](mailto:huazhenliu@sjtu.edu.cn)

3 Department of Oral and Craniomaxillofacial Surgery, Shanghai Ninth People's Hospital, Shanghai Jiao Tong University School of Medicine; College of Stomatology, Shanghai Jiao Tong University; National Center for Stomatology; National Clinical Research Center for Oral Diseases, Shanghai Key Laboratory of Stomatology; Shanghai Research Institute of Stomatology, Shanghai, 200011, China. E-mail: [kouqiangzy@sjtu.edu.cn](mailto:kouqiangzy@sjtu.edu.cn)

4 Department of Oral and Craniomaxillofacial Surgery, Shanghai Ninth People's Hospital, Shanghai Jiao Tong University School of Medicine; College of Stomatology, Shanghai Jiao Tong University; National Center for Stomatology; National Clinical Research Center for Oral Diseases, Shanghai Key Laboratory of Stomatology; Shanghai Research Institute of Stomatology, Shanghai, 200011, China. E-mail: [qiansexingqiutlr123@sjtu.edu.cn](mailto:qiansexingqiutlr123@sjtu.edu.cn)

5 School of Electronic Information and Electrical Engineering, Shanghai Jiao Tong University, Shanghai, China. E-mail: [xinyu.xu@sjtu.edu.cn](mailto:xinyu.xu@sjtu.edu.cn)

6 School of Mathematics and Statistics, Lanzhou University, Lanzhou, 730000, China. E-mail: [shiyt2024@lzu.edu.cn](mailto:shiyt2024@lzu.edu.cn)

7 Faculty of Dentistry, The University of Hong Kong, Hong Kong, Hong Kong SAR, China. E-mail: [chengmj@connect.hku.hk](mailto:chengmj@connect.hku.hk)

8 Department of Oral and Craniomaxillofacial Surgery, Shanghai Ninth People's Hospital, Shanghai Jiao Tong University School of Medicine; College of Stomatology, Shanghai Jiao Tong University; National Center for Stomatology; National Clinical Research Center for Oral Diseases, Shanghai Key Laboratory of Stomatology; Shanghai Research Institute of Stomatology, Shanghai, 200011, China. E-mail: [wangym99@sjtu.edu.cn](mailto:wangym99@sjtu.edu.cn)

9 Department of Oral and Craniomaxillofacial Surgery, Shanghai Ninth People's Hospital, Shanghai Jiao Tong University School of Medicine; College of Stomatology, Shanghai Jiao Tong University; National Center for Stomatology; National Clinical Research Center for Oral Diseases, Shanghai Key Laboratory of Stomatology; Shanghai Research Institute of Stomatology, Shanghai, 200011, China. E-mail: [little-ku@sjtu.edu.cn](mailto:little-ku@sjtu.edu.cn)

10 Department of Oral and Craniomaxillofacial Surgery, Shanghai Ninth People's Hospital, Shanghai Jiao Tong University School of Medicine; College of Stomatology, Shanghai Jiao Tong University;

National Center for Stomatology; National Clinical Research Center for Oral Diseases, Shanghai Key Laboratory of Stomatology; Shanghai Research Institute of Stomatology, Shanghai, 200011, China. E-mail: [zt\\_fiona@sjtu.edu.cn](mailto:zt_fiona@sjtu.edu.cn)

11 Department of Oral and Craniomaxillofacial Surgery, Shanghai Ninth People's Hospital, Shanghai Jiao Tong University School of Medicine; College of Stomatology, Shanghai Jiao Tong University; National Center for Stomatology; National Clinical Research Center for Oral Diseases, Shanghai Key Laboratory of Stomatology; Shanghai Research Institute of Stomatology, Shanghai, 200011, China. E-mail: [yilang\\_du@sjtu.edu.cn](mailto:yilang_du@sjtu.edu.cn)

12 Department of Oral and Craniomaxillofacial Surgery, Shanghai Ninth People's Hospital, Shanghai Jiao Tong University School of Medicine; College of Stomatology, Shanghai Jiao Tong University; National Center for Stomatology; National Clinical Research Center for Oral Diseases, Shanghai Key Laboratory of Stomatology; Shanghai Research Institute of Stomatology, Shanghai, 200011, China. E-mail: [chancy-s@sjtu.edu.cn](mailto:chancy-s@sjtu.edu.cn)

13 Department of Oral and Craniomaxillofacial Surgery, Shanghai Ninth People's Hospital, Shanghai Jiao Tong University School of Medicine; College of Stomatology, Shanghai Jiao Tong University; National Center for Stomatology; National Clinical Research Center for Oral Diseases, Shanghai Key Laboratory of Stomatology; Shanghai Research Institute of Stomatology, Shanghai, 200011, China. E-mail: [114068@sh9hospital.org.cn](mailto:114068@sh9hospital.org.cn)

14 School of Biomedical Engineering, Shanghai Jiao Tong University, Shanghai, China. E-mail: [xiangsuncheng17@sjtu.edu.cn](mailto:xiangsuncheng17@sjtu.edu.cn)

15 Department of Oral and Craniomaxillofacial Surgery, Shanghai Ninth People's Hospital, Shanghai Jiao Tong University School of Medicine; College of Stomatology, Shanghai Jiao Tong University; National Center for Stomatology; National Clinical Research Center for Oral Diseases, Shanghai Key Laboratory of Stomatology; Shanghai Research Institute of Stomatology, Shanghai, 200011, China. E-mail: [yuhb1057@sh9hospital.org.cn](mailto:yuhb1057@sh9hospital.org.cn)

---

# Jiahao Bao, Huazhen Liu and Yu Zhuang have contributed equally to this work and shared co-first authorship.

\* Hongbo Yu, Suncheng Xiang and Shunyao Shen have contributed equally as senior last author.

### **Corresponding author**

Hongbo Yu, Professor, DDS, MD

Department of Oral & Craniomaxillofacial Surgery,

Shanghai Ninth People's Hospital,

Shanghai Jiao Tong University School of Medicine.

Tel: 021-23271699-5144

E-mail: [yuhb1057@sh9hospital.org.cn](mailto:yuhb1057@sh9hospital.org.cn)

### **Acknowledgements**

This study was supported by National Natural Science Foundation of China (81571022), Shanghai

Natural Science Foundation (23ZR1438100) and AI Interdisciplinary Research Program of Shanghai Ninth People's Hospital (JYJC2025010).

### **Declaration of competing interests**

The authors declare that they have no known competing financial interests or personal relationships that could have appeared to influence the work reported in this paper.

### **CREDIT Author Statement**

Jiahao Bao: Conceptualization, Data Curation, Methodology, Formal Analysis, Investigation, Visualization, Writing - Original Draft. Huazhen Liu: Data Curation, Methodology, Formal Analysis, Software, Investigation, Validation, Writing - Original Draft. Yu Zhuang: Data Curation, Methodology, Investigation, Validation, Writing- Reviewing and Editing. Leran Tao, Xinyu Xu, Yongtao Shi: Data Curation, Methodology, Visualization, Writing- Reviewing and Editing. Mengjia Cheng, Yiming Wang, Congshuang Ku: Data curation, Investigation, Software, Validation, Writing- Reviewing and Editing. Ting Zeng, Yilang Du, Siyi Chen: Data curation, Validation, Writing- Reviewing and Editing. Shunyao Shen, Suncheng Xiang: Conceptualization, Investigation, Supervision, Resources, Writing- Reviewing and Editing. Hongbo Yu: Conceptualization, Investigation, Supervision, Resources, Project administration, Funding Acquisition, Writing- Reviewing and Editing.

### **Ethics approval and consent to participate**

The study was performed after approval by the ethics committee of Shanghai Ninth People's Hospital, Shanghai Jiao Tong University School of Medicine (IRB No. SH9H-2022-TK12-1). Informed consent was obtained from all participants or their guardians.

### **Data Statements**

The de-identified data and source code used and/or analyzed during the current study are available from the corresponding author upon reasonable request.

# PhysSFI-Net: Physics-informed Geometric Learning of Skeletal and Facial Interactions for Orthognathic Surgical Outcome Prediction

Jiahao Bao<sup>1#</sup>, Huazhen Liu<sup>2#</sup>, Yu Zhuang<sup>3#</sup>, Lieran Tao<sup>4</sup>, Xinyu Xu<sup>5</sup>, Yongtao Shi<sup>6</sup>, Mengjia

Cheng<sup>7</sup>, Yiming Wang<sup>8</sup>, Congshuang Ku<sup>9</sup>, Ting Zeng<sup>10</sup>, Yilang Du<sup>11</sup>, Siyi Chen<sup>12</sup>, Shunyao

Shen<sup>13\*</sup>, Suncheng Xiang<sup>14\*</sup>, Hongbo Yu<sup>15\*</sup>

# Jiahao Bao, Huazhen Liu and Yu Zhuang have contributed equally to this work and shared co-first authorship.

\* Hongbo Yu, Suncheng Xiang and Shunyao Shen have contributed equally as senior last author.

## Abstract

Orthognathic surgery repositions jaw bones to restore occlusion and enhance facial aesthetics. Accurate simulation of postoperative facial morphology is essential for preoperative planning. However, traditional biomechanical models are computationally expensive, while geometric deep learning approaches often lack interpretability. In this study, we develop and validate a physics-informed geometric deep learning framework named PhysSFI-Net for precise prediction of soft tissue deformation following orthognathic surgery. PhysSFI-Net consists of three components: (1) a hierarchical graph module with craniofacial and surgical plan encoders combined with attention mechanisms to extract skeletal-facial interaction features; (2) a Long Short-term Memory Networks (LSTM)-based sequential predictor for incremental soft tissue deformation; (3) and a biomechanics-inspired module for high-resolution facial surface reconstruction. Model performance was assessed using point cloud shape error (Hausdorff Distance), surface deviation error and landmark localization error (Euclidean distances of craniomaxillofacial landmarks) between predicted facial shapes with corresponding ground truths. A total of 135 patients who underwent orthodontic and orthognathic joint treatment were included for model training and validating. Quantitative analysis demonstrated that PhysSFI-Net achieved a point cloud shape error of  $1.070 \pm 0.088$  mm, a surface deviation error of  $1.296 \pm 0.349$  mm, and a landmark localization error of  $2.445 \pm 1.326$  mm. Comparative experiments indicated that PhysSFI-Net outperformed the state-of-the-art method ACMT-Net in prediction accuracy ( $P < 0.05$ ). In conclusion, PhysSFI-Net enables interpretable, high-resolution prediction of postoperative facial morphology with superior accuracy, showing strong potential for clinical application in orthognathic surgical planning and simulation.

**Keywords:** Dento-maxillofacial Deformities; Orthognathic Surgery; Virtual Surgical Planning; Facial Deformation Prediction

## 1. Introduction

Dento-maxillofacial deformities, characterized by dysfunctions in the stomatognathic system and abnormal facial morphology, significantly impact patients' physiological functions and mental

well-being(Dunworth et al., 2024). Orthognathic surgery (OGS) corrects jaw deformities by performing osteotomies and repositioning bone segments of the maxilla and mandible, thereby restoring occlusal function and enhancing facial aesthetics(Naran et al., 2018). The preoperative optimization of the surgical plan is a crucial determinant of successful outcomes in OGS(Xia et al., 2015). Computer-Assisted Surgical Simulation (CASS) provides clinicians with powerful tools for virtual surgery and decision support. By reconstructing three-dimensional (3D) maxillofacial models, it enables comprehensive evaluation of anatomical structures and allows precise simulation of osteotomies and bony segment movements, thus facilitating the identification of optimal surgical strategies(Hsu et al., 2013; Wang et al., 2025). During the process of CASS, occlusion can be accurately simulated through dental model articulation due to the rigid contact relationship between teeth(Ho et al., 2019). However, the deformation of facial soft tissues following skeletal movement remains challenging to precisely predict, owing to the nonlinear and complex biomechanical relationship between soft tissues and underlying bony structures(Pellitteri et al., 2025). This leads to surgical planning decisions that lack objective criteria and are highly reliant on clinical experience. Hence, there is an urgent need for developing an accurate and effective predictive approach.

In clinical practice, some surgical planning software offers a soft tissue prediction function for visualizing treatment objective, which lack sufficient accuracy to guide surgical skeletal movement decisions(Xie et al., 2026; Xing et al., 2023). Various efforts have been made to achieve precise facial soft tissue deformation predictions in orthognathic surgery(Hertanto et al., 2021). Current methodologies primarily include sparse landmark-based approaches and biomechanical modeling techniques. Sparse landmark-based approaches typically estimate bone-to-soft-tissue displacement ratios derived from clinical observations or machine learning algorithms, and they are commonly employed for predictions based on two-dimensional imaging data(Cho et al., 2024). In contrast, biomechanical modeling approaches, including mass spring models, mass tensor models, and finite element models (FEM), facilitate simulations of complex and nonlinear tissue deformation patterns(Cheng et al., 2022; Lampen et al., 2022). Among these, FEM effectively integrates the biomechanical properties of craniofacial tissues with patient-specific anatomical data. By utilizing precise interpolation methods to calculate the deformation gradient within each element, FEM robustly simulates complex nonlinear biomechanical behaviors, which is widely recognized as the most accurate and reliable technique for predicting facial soft-tissue changes(Chabanas et al., 2003; Mollemans et al., 2007). Kim et al. developed a multi-stage FEM simulation method that incorporates realistic tissue sliding to enhance prediction accuracy(D. Kim et al., 2017). Subsequently, they applied an incremental simulation approach with a realistic lip-sliding mechanism, significantly improving the prediction accuracy in the lip region(D. Kim et al., 2021). Ruggiero et al. established a facial soft-tissue model incorporating detailed musculature structures and employed FEM to simulate postoperative facial morphology(Ruggiero et al., 2022, 2023). Although FEM demonstrates high prediction accuracy, a single simulation typically requires approximately 30 minutes to complete. Moreover, the complexity of FEM increases with anatomical detail, resulting in substantial computational demands and extended processing times, posing

substantial challenges for meeting the demands of clinical applications(Lampen et al., 2022, 2024).

Recently, the application of artificial intelligence (AI) has significantly transformed the landscape of clinical medicine (Khalid et al., 2024; Liang et al., 2026; Lin et al., 2025; Zheng et al., 2026). Many data-driven deep learning (DL) algorithms have been developed as a promising alternative for traditional biomechanical methods, achieving faster and comparable accurate predictions(Bao et al., 2024, 2025; R. Zhang et al., 2025). Ter Horst et al. developed an autoencoder-based algorithm to predict soft tissue changes following mandibular advancement surgery. Ma et al. first proposed the FSC-Net to learn the nonlinear mapping from skeletal changes to facial shape responses(Ma et al., 2023). Fang et al. proposed the Attentive Correspondence assisted Movement Transformation network (ACMT-Net) to predict postoperative facial shapes by calculating point-to-point attention correspondence matrices between bone and facial point sets, clarifying spatial relationships between facial soft tissue and bone(Fang et al., 2022, 2024). Considering biomechanical properties, Lampen et al. developed a biomechanics-informed model based on the PointNet++ architecture, which integrates facial mesh geometry, bone segment displacement, and FEM boundary conditions as inputs to predict deformation. Nevertheless, current deep learning methods for facial prediction continue to face several notable limitations. First, previous studies frequently utilize small size datasets (approximately 50 cases), overlooking the diverse range of deformity characteristics and surgical approaches, which limits the models' potential for generalization. Second, model interpretability remains insufficient, as the absence of biomechanical priors in geometric reasoning hampers the clarity of underlying predictive mechanisms for clinical decision-making. Finally, point cloud-based processing often leads to increased noise and information loss on the surface, compromising the quality of three-dimensional facial reconstructions.

To address the limitations identified in previous models, we developed a novel deep-learning framework named the Physics-Informed Skeletal-Facial Interaction Network (PhysSFI-Net) for orthognathic postoperative facial shape prediction, which was inspired by the biomechanical processes underlying soft tissue deformation. Through comprehensive validation using multiple quantitative metrics, our model has demonstrated superior performance compared to existing state-of-the-art methods. Our study contributes significantly in several aspects: (1) We introduced a hierarchical graph representation method to encode and extract geometric topological relationships between facial and skeletal structures and surgical plans, combined with an attention mechanism to predict the geometric features of facial displacement fields effectively. (2) We designed a novel LSTM-based soft tissue deformation prediction module, which accurately models the complex and continuous deformation processes induced by mechanical forces, thereby improving prediction accuracy. (3) Recognizing information loss inherent in point cloud down-sampling, we developed an electromechanics-informed high-precision reconstruction approach capable of rapidly generating postoperative facial meshes without compromising reconstruction accuracy.

## 2. Materials and methods

## 2.1. Study design

The overview of the study pipeline is shown in **Fig.1**. Our study adheres to the Checklist for Artificial Intelligence in Dental Research. The study was performed in accordance with the Declaration of Helsinki and this study was approved by the ethics committee (IRB No. xxx).

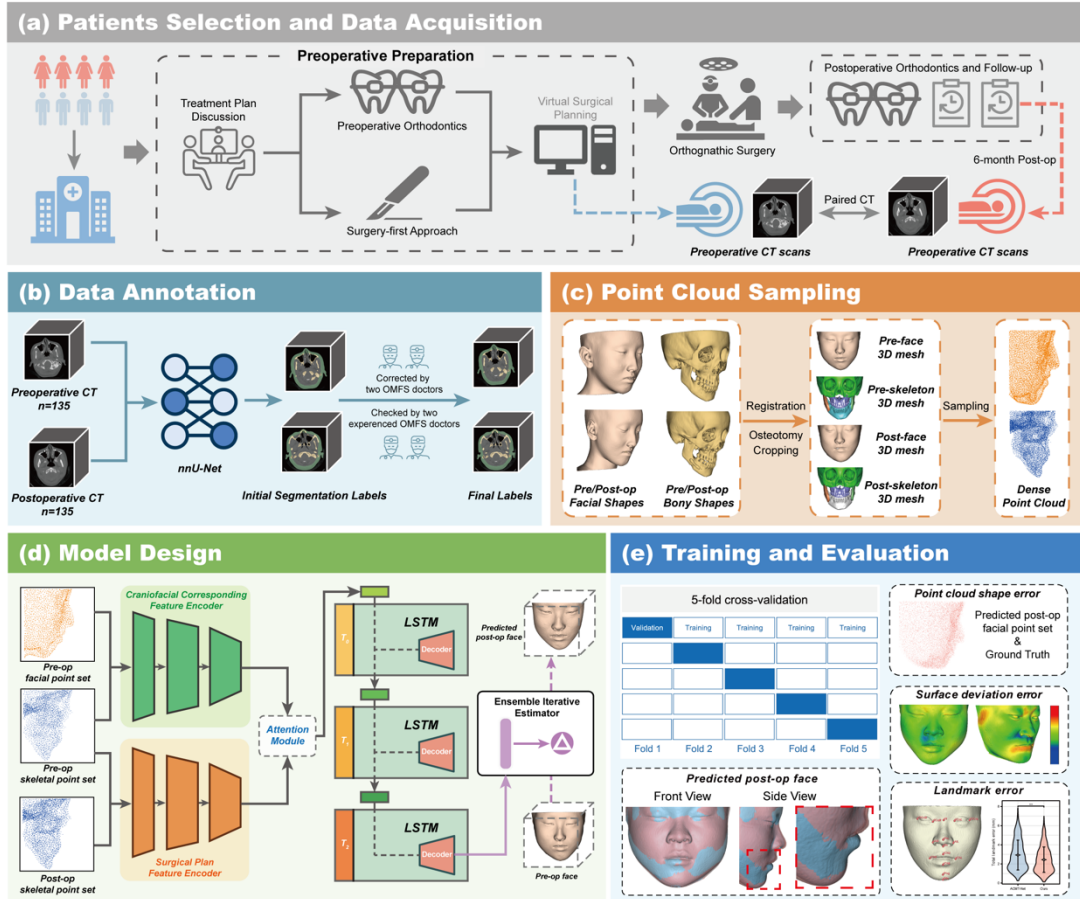


**Figure 1. The overview of the study pipeline. (a) Patient selection and data acquisition. (b) Data annotation. (c) Point cloud sampling. (d) Model design. (e) Training and evaluation.**

## 2.2 Data acquisition

This study retrospectively enrolled patients diagnosed with skeletal malocclusion from Department of XXX, all of whom underwent comprehensive orthodontic and orthognathic combined treatment including treatment plan discussion, preoperative preparation, virtual surgical planning, and complete postoperative follow-up. Patients with congenital dentofacial deformities (n = 12), those who underwent additional soft-tissue cosmetic procedures (n = 18), or those with facial prostheses such as polyether ether ketone (PEEK) implants (n = 15) were excluded from the study. All CMF CT scans were required to meet predefined quality standards. Cases with severe metal artifacts or poor overall image quality were excluded (n = 10). Preoperative CT data were acquired during the virtual surgical planning phase, approximately one month before surgery, when patients had completed preoperative orthodontic treatment and their teeth and skeletal structures were stabilized. Paired postoperative CT scans were collected six months after surgery, at which point

soft-tissue swelling had fully resolved (**Fig.1a**).

## 2.3 Data Annotation and Preprocessing

CT scans were obtained as DICOM format. A semi-automated workflow was utilized for segmenting craniofacial skeletal and soft-tissue structures. A pretrained nnU-Net model were employed to generate initial segmentation masks, which were then carefully refined slice by slice at the voxel level by two oral and maxillofacial surgeons. After verification by two expert clinicians, the final segmentation results were confirmed (**Fig.1b**). Due to variations in patient positioning and the extent of CT coverage, each segmentation was cropped to retain only regions relevant to orthognathic procedures. All tissues posterior to the anterior margin of the external auditory canal and superior to the supraorbital rim were deleted using 3D Slicer software (version 5.0.2). Then, all patient skeleton and face data were registered to a unified coordinate system. For each patient, we employed an Iterative Closest Point (ICP) algorithm to align paired preoperative and postoperative model using stable landmarks (e.g., nasion, medial canthus, and lateral canthus). A paired dataset was established which consists of preoperative and postoperative craniofacial skeletal models and soft tissue surfaces.

Subsequently, we acquired pointwise displacement data of skeletal segments through the following methodological workflow: (1) The preoperative skeletal model was imported into Mimics software and segmented according to standard orthognathic surgical procedures. The segmentation resulted in distinct cranial, maxillary, mandibular body, and bilateral mandibular ramus segments. For patients who underwent genioplasty, an additional chin segment was also isolated. (2) The postoperative skeletal model was then imported and precisely registered to the preoperative model utilizing cranial anatomical landmarks as references. The preoperative skeletal segments were individually translated and rotated, ensuring each segment accurately aligned with the corresponding postoperative segment positions. (3) The repositioned skeletal segments were merged with the cranial segment to generate a surgical planning skeletal model. This approach ensured pointwise correspondence in the sampled bone point clouds and maintained complete conformity with the postoperative skeletal anatomy. In addition, in consideration of GPU memory, the 3D meshes were down-sampled into dense point clouds that represent both bony and facial soft-tissue structures (**Fig.1c**, **Fig.2a**).

## 2.4 Model Description

### 2.4.1 Overall architecture and task restatement

The overall architecture of our proposed model, named PhysSFI-Net, is illustrated in **Fig. 2b-d**. PhysSFI-Net comprises three primary components: (1) A hierarchical graph representation module, consisting of a craniofacial correspondence feature encoder and a surgical plan feature encoder, combined with an attention mechanism designed to predict facial displacement features (**Fig.2b**). (2) A sequential prediction approach that employs three Long Short-term Memory Networks (LSTM) modules to simulate incremental soft tissue deformation guided by mechanical states (**Fig.2c**). (3) An electromechanics-inspired high-precision reconstruction method, facilitating accurate 3D reconstruction of postoperative facial morphology (**Fig.2d**).

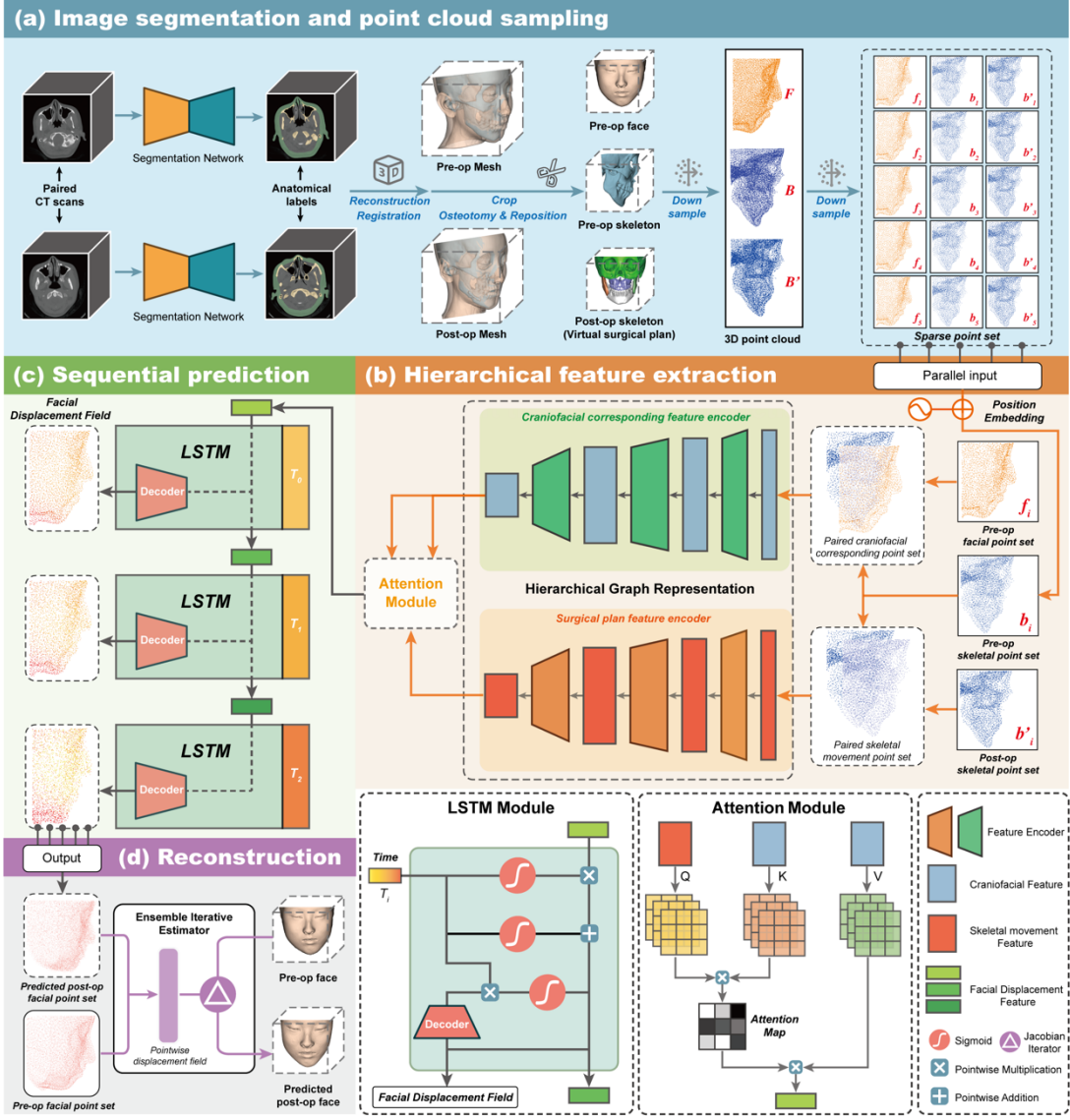


**Figure 2. The detailed architecture of Physics-Informed Skeletal-Facial Interaction Network (PhysSFI-Net).** (a) Image segmentation and point cloud sampling. (b) A hierarchical feature extraction approach, consisting of a craniofacial correspondence feature encoder and a surgical plan feature encoder, combined with an attention mechanism designed to predict facial displacement features. (c) A sequential prediction approach that employs three LSTM modules to simulate incremental soft tissue deformation guided by mechanical states. (d) An electromechanics-inspired high-precision reconstruction method, facilitating accurate 3D reconstruction of postoperative facial morphology.

We formulate the postoperative facial shape prediction task using point clouds as the primary data structure. Given the preoperative skeletal shape  $B = \{b_i \in \mathbb{R}^3\}_{i=1}^{N_B}$ , the postoperative skeletal shape  $B' = \{b'_i \in \mathbb{R}^3\}_{i=1}^{N_B}$ , and the preoperative facial surface  $F = \{f_j \in \mathbb{R}^3\}_{j=1}^{N_F}$ , the goal is to predict the postoperative facial surface  $F' = \{f'_j \in \mathbb{R}^3\}_{j=1}^{N_F}$  by learning a mapping  $\Phi$ :

$$F' = \Phi(B, B', F) = F + \Delta F(B, B', F) \quad (1)$$

To comprehensively and accurately capture the structured information embedded within the point

cloud data, we adopt a geometric-topological perspective by modeling the point cloud as a 2D manifold embedded in 3D space. This modeling paradigm aims to explicitly characterize the local manifold properties of point clouds, thereby enabling the extraction of rich geometric structures inherently encoded in the data. Accordingly, the mapping  $\Phi$  can be interpreted as a transformation between manifolds, facilitating a geometry-aware prediction of soft tissue deformation:

$$\Phi: \mathcal{M}_B \times \mathcal{M}_{B'} \times \mathcal{M}_F \rightarrow \mathcal{M}_{F'} \quad (2)$$

In this context, Equation (1) can be regarded as the discrete sampling form of the underlying continuous manifold mapping.

#### 2.4.2 Hierarchical feature extraction

To enhance computational efficiency, the input point cloud is partitioned into five low-resolution sub-clouds, which are processed in parallel. After obtaining the predicted displacement fields for each sub-cloud, we perform high-resolution reconstruction to generate the final output. Each sub-cloud consists of three components: the preoperative skeletal point cloud, the postoperative skeletal point cloud, and the preoperative facial point cloud. These heterogeneous point clouds are uniformly represented as a label-augmented manifold structure, which we define as an enhanced manifold representation. This representation encodes both geometric information and semantic identity (e.g., anatomical source) of each point, enabling the network to jointly learn across structurally distinct yet spatially correlated modalities:

$$\mathcal{M}(p_i) = \{(g_i, \ell_i) | p_i \in \mathbb{R}^3, \ell_i \in \{0,1\}^3\} \quad (3)$$

where  $P_i$  denotes the 3D coordinates of skeletal or facial point clouds, while  $g_i$  is a function of the input location, encoding the local graph structure of the underlying manifold:

$$g_i = \sum_{j \in \mathcal{N}(i)} w_{ij} \phi(p_j, p_i - p_j), \mathcal{N}(i) = KNN(p_i) \quad (4)$$

Here, the label  $\ell_i$  serves as a positional encoding for each point in the point cloud, providing additional spatial context to guide the learning of manifold-aware features:

$$l_i(p_i) = \begin{cases} \sin\left(\frac{p_i}{10000^{2k/C}}\right) & i = 2k \\ \cos\left(\frac{p_i}{10000^{2k/C}}\right) & i = 2k + 1 \end{cases} \quad (5)$$

where  $k = 0, 1, 2, \dots, \lfloor C/2 \rfloor - 1$ . Heterogeneous point clouds are treated as an integrated entity rather than being processed separately, enabling more effective capture of local geometric relationships across different anatomical structures. The network consists of two primary components: feature extraction and facial surface reconstruction. The feature extraction module (**Fig.2b**) is designed to encode skeletal displacement and model the skeletal-to-facial correspondence. A hierarchical PointNet-based architecture is employed to extract structural features, while graph convolutional layers are incorporated to further capture local topological dependencies (**Fig.S1**) (J. Zhang et al., 2025). Upon obtaining the encoded skeletal displacement features and skeletal-facial relational features, we introduce a multi-head attention mechanism to perform hierarchical feature extraction. In each attention layer, the facial surface features serve as the query ( $Q_h$ ), the skeletal-facial relational features as the key ( $K_h$ ), and the skeletal displacement features as the value ( $V_h$ ). Attention maps are computed to aggregate geometry-aware features,

resulting in refined representations for facial shape prediction:

$$\mathbf{A}_h = \text{softmax} \left( \frac{\mathbf{Q}_h \mathbf{K}_h^T}{\sqrt{d_h}} + \mathbf{E}_h \right) \mathbf{V}_h \quad (6)$$

Here,  $E_h$  denotes the relative positional encoding, which introduces geometric priors into the attention mechanism by capturing spatial relationships between query and key points.

#### 2.4.3 Sequential prediction based on LSTM

To simulate the physically constrained postoperative deformation process, we employ an LSTM-based decoder that iteratively generates the facial displacement field (**Fig 2c**). At each time step  $t \in \{0, 1, \dots, T-1\}$ , the decoder outputs an incremental displacement vector  $\delta^t \in \mathbb{R}^{N_F \times 3}$ . The final predicted displacement field is then obtained by summing the outputs across all time steps:

$$\Delta f = \sum_t \delta^t \quad (7)$$

The iterative process of the LSTM decoder is designed to simulate the continuous evolution of soft tissue deformation. At each time step, the decoder takes the current time index, feature representation, and intermediate displacement field as input, and outputs the updated feature state and displacement increment. Formally, the process can be described as:

$$[x^t; \delta^t] = \text{LSTM}[t; x^{t-1}; \delta^{t-1}] \quad (8)$$

The iterative process is initialized at  $t=0$ ,  $x^0 = \bigoplus_h A_h$ , and  $\delta^0 = 0$ .

#### 2.4.4 High-Resolution Reconstruction

High-resolution reconstruction of post-operative facial soft tissue requires balancing physical plausibility with clinical real-time requirements. We present a graph-based Ensemble Iterative Estimator that integrates elasticity-inspired regularization into neural network predictions through a mesh-free graph optimization framework to reduce computational complexity (**Fig 2d**). The method converts the post-operative facial 3D point cloud  $F' = \{f_j' \in \mathbb{R}^3\}_{j=1}^{N_F}$  into a graph structure model  $G = (V, E)$  with local neighborhood topological connections. Edge weights are assigned via a Gaussian kernel

$$\omega_{ij} = \exp(-\|\delta_i - \delta_j\|^2 / (2\sigma_i^2)) \quad (9)$$

to encode both the local stiffness of soft tissues and spatial information within the point cloud.

The displacement field is obtained by solving the constrained system

$$L_G \boldsymbol{\delta} = 0, \text{ s.t. } \boldsymbol{\delta}|_S = \boldsymbol{\delta}_{\text{fix}}, \quad (10)$$

where the constrained point set  $S$  consists of spatial points where displacement is fixed to  $\boldsymbol{\delta}_{\text{fix}}$  predicted by neural network, and  $L_G$  denotes the graph Laplacian operator:

$$(L_G \boldsymbol{\delta})_{ij} = \begin{cases} \sum_{k \in N(i)} \omega_{ik}, & i = j, \\ -\omega_{ij}, & i \neq j \wedge j \in N(i), \\ 0, & \text{otherwise.} \end{cases} \quad (11)$$

This formulation arises from combining deformation continuity constraints through local neighborhood coupling with neural network-predicted displacement preservation.

When setting  $\sigma_i$  as the mean nodal distance  $h$ , the graph Laplacian operator converges to the

continuous Laplacian operator(Singer, 2006)

$$\frac{1}{h^2} (L_G \delta)_i = \sum_j \omega_{ij} (\delta_i - \delta_j) \xrightarrow{h \rightarrow 0^+} C \Delta \delta(x_i), \quad (12)$$

which under near-incompressibility conditions of biological tissues predominantly governs shear effects in elastic deformation(Chagnon et al., 2015). This heuristic discretization choice inherently captures shear-dominated deformation patterns through its operator properties, while maintaining mathematical consistency with biomechanical principles.

For efficient computation, we implement a Jacobi relaxation iteration (**Fig.S2**) scheme:

$$\delta_i^{(n+1)} = \frac{1}{(L_G)_{ii}} \left( \sum_{j \in N(i) \cap S} \omega_{ij} \delta_j + \sum_{k \in N(i) \setminus S} \omega_{ik} \delta_k^{(n)} \right), \quad (13)$$

where  $N(i)$  denotes the neighborhood of point  $x_i$ . This iterative process essentially propagates displacements from known to unknown points.

Notably, even when neural network predictions  $\delta_{\text{fix}}$  exhibit non-zero deviations from biomechanical priors (resulting in residual terms in the harmonic equation's RHS), the relaxation method effectively reconciles prediction results with mechanical constraints through its robust convergence behavior, thereby achieving rapid high-fidelity facial reconstruction.

The algorithm initializes unknown point weights through neighborhood averaging. Each iteration processes only local neighborhoods with an average size  $k$  accounting for 0.05% of the total point cloud  $N$ , achieving  $O(kN)$  complexity. Experimental validation confirms millimeter-scale accuracy within 5 iterations, demonstrates performance advantages in processing  $O(10^5)$ -scale point clouds. By embedding biomechanical principles into a high-efficiency computational framework, this method establishes a novel paradigm for rapid reconstruction of diverse facial morphologies.

#### 2.4.5 Combination of multiple loss functions

The network is trained using a combination of loss functions. The first component is a displacement field distance constraint, formulated as the Chamfer Distance between the predicted postoperative facial point cloud and the ground-truth surface:

$$L_{CD} = \frac{1}{N_F} \left( \sum_{f_i \in F} \min_{f'_j \in F'} \|f_i + \Delta f_i - f'_j\|^2 + \sum_{f'_j \in F'} \min_{f_i \in F} \|f_i + \Delta f_i - f'_j\|^2 \right) \quad (14)$$

Additionally, a smoothness regularization term is introduced to promote gradual, spatially coherent deformations:

$$L_{smooth} = \frac{1}{N} \sum_{i=1}^N \sum_{j \in N(i)} \|\Delta f_i - \Delta f_j\| \quad (15)$$

Finally, since only the final displacement field is explicitly supervised, while intermediate states in the LSTM decoding process remain unobserved, we introduce a weak supervision constraint to enforce directional consistency across the iterative steps. Specifically, we encourage the displacement increments at each time step to align with the overall deformation direction. The loss is defined as:

$$L_{prog} = \frac{1}{T} \sum_{t=0}^{T-1} \left\| \sum_{k=0}^t \delta^k - \Delta f_{pseudo}^t \right\|^2, \quad \Delta f_{pseudo}^t = \frac{t}{T-1} \Delta f \quad (16)$$

## 2.5 Model Evaluation

To comprehensively evaluate the predictive performance of PhysSFI-Net, multiple quantitative metrics were employed. First, for the predicted facial point clouds, the Hausdorff distance between the ground truth postoperative facial shapes and the predicted point clouds was calculated to quantify the shape accuracy. Second, for reconstructed 3D facial meshes, the average surface deviation error between the ground truth mesh and the reconstructed mesh from the model predictions was computed. These mesh deviation errors were visualized using heatmaps with a color scale ranging from -4.00 mm to +4.00 mm, providing intuitive spatial information about prediction accuracy. Third, to assess landmark prediction accuracy, we selected 19 clinically significant facial landmarks in the periorbital, midface, perioral, and chin regions. Experienced clinicians independently annotated these landmarks on both the ground truth and the predicted facial meshes, and Euclidean distances between corresponding landmarks were computed within a common coordinate system. Since landmark errors less than 2 mm are typically considered clinically acceptable, we calculated and reported the proportions of landmark prediction errors falling within three ranges: less than 2 mm, between 2 and 4 mm, and greater than 4 mm.

For comparative analysis, we reproduced Attentive Correspondence assisted Movement Transformation network (ACMT-Net), a state-of-the-art facial shape prediction method, following the authors' original specifications. We then directly compared PhysSFI-Net with ACMT-Net across all the aforementioned metrics.

## 2.6 Training Details and Statistics Analysis

We implemented our model using PyTorch library. The network was trained using the Adam optimizer on an NVIDIA A100 GPU with 80 GB of memory. The batch size was set to 8 for all experiments. **Figure 3** showed the loss-epoch curve for model training of PhysSFI-Net. All statistical analyses were performed by R software (Version 4.1.2). Categorical variables were presented in the form of numbers and percentages, while continuous variables were presented as means  $\pm$  standard deviations. For the comparison of continuous variables between two groups, the T-test was employed for normally distributed continuous variables, and the Wilcoxon rank-sum tests were used for non-normally distributed continuous variables. A *P* value of less than 0.05 was regarded as statistically significant.

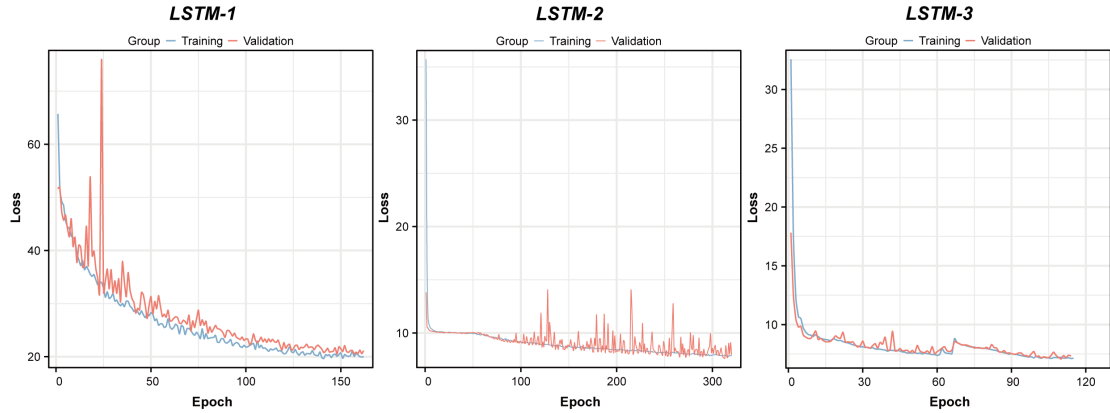


**Figure 3.** Training and validation logs of PhysSFI-Net under different numbers of LSTM layers.

### 3. Results

#### 3.1 Participants and clinical characteristics

We retrospectively enrolled patients diagnosed with skeletal malocclusion from Department XXXX, all of whom underwent comprehensive orthodontic and orthognathic combined treatment including treatment plan discussion, preoperative preparation, virtual surgical planning, and complete postoperative follow-up. Following the inclusion and exclusion criteria, a total of 135 patients were included in the study. Comprehensive clinical characteristics (gender, age, body mass index, skeletal discrepancy, facial asymmetry, Frankfort horizontal plane-mandibular plane angle) and surgery types (Le Fort I osteotomy, bilateral sagittal split ramus osteotomy, genioplasty, paranasal bone grafting) are summarized in **Fig.4** and detailed in **Table S1**. Among the participants, 68.1% were female, and the majority presented with a normal BMI ( $18.5 \leq \text{BMI} \leq 25$ ). Consistent with the prevalence patterns observed in the Chinese population, Class III skeletal malocclusion accounted for the largest proportion of cases (73.3%), followed by Class II (17.8%). Facial asymmetry was identified in 61.5% of patients, and 56.3% exhibited a high-angle facial morphology (**Fig.4a**). In terms of surgical types, 74 patients underwent a combined Le Fort I osteotomy and BSSRO, with 14 of these also receiving concomitant genioplasty (**Fig.4b–c**). To improve midfacial projection, a subset of patients underwent paranasal bone grafting during orthognathic surgery. A schematic overview of the surgical procedures is provided in **Fig.4d**.

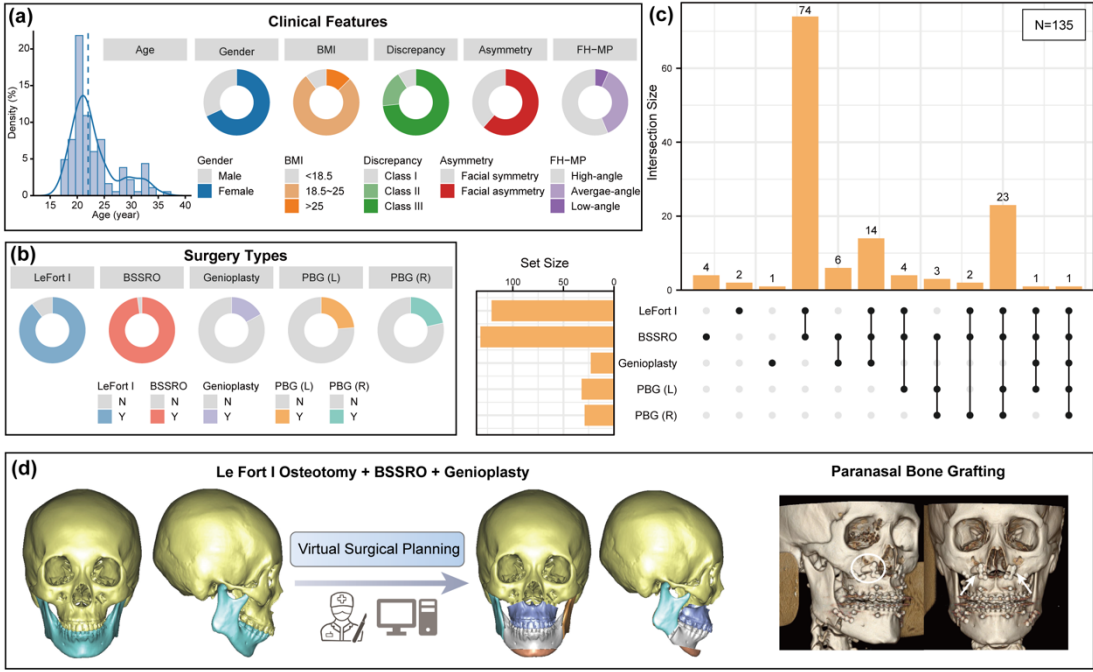


**Figure 4. Summary of patient characteristics and surgical procedures.** (a) Clinical features of 135 patients, including age, gender, BMI, skeletal discrepancy, facial asymmetry, and vertical facial type. (b) Types of orthognathic procedures performed, including Le Fort I osteotomy, BSSRO, genioplasty, and paranasal bone grafting. (c) Distribution of surgical combinations across the dataset shown using an Upset plot. (d) Example of virtual surgical planning workflow.

### 3.2 Experiments and Model Performance

To comprehensively evaluate the model's performance, multiple quantitative metrics were employed. The Hausdorff Distance (HD) between the predicted facial point set and the ground truth was calculated to quantify shape discrepancies of 3D point clouds. Additionally, surface deviation errors and landmark errors between the predicted and ground truth meshes were utilized as quantitative indicators for assessing the accuracy of the reconstructed 3D facial meshes. We reproduced the state-of-the-art facial shape prediction model ACMT-Net on our dataset by following the implementation details described in their original publication, which was used as comparative baselines to evaluate the performance of our proposed approach(Fang et al., 2022, 2024).

In our work, we first integrated the preoperative facial point cloud with both preoperative and postoperative skeletal point clouds in order to predict postoperative facial appearance. This enabled the generation of five sets of sparse predictions, which were subsequently fused into a unified dense point cloud representation. Compared to the current state-of-the-art model, PhysSFI-Net consistently demonstrated lower prediction errors across all five sparse prediction sets (**Fig.5a**; **Table S2**). As illustrated in **Fig.5c-d**, PhysSFI-Net achieved superior dense point cloud reconstruction accuracy, with a significantly reduced error (PhysSFI-Net:  $1.070 \pm 0.088$  mm vs. ACMT-Net:  $1.186 \pm 0.080$  mm;  $P < 0.05$ ).

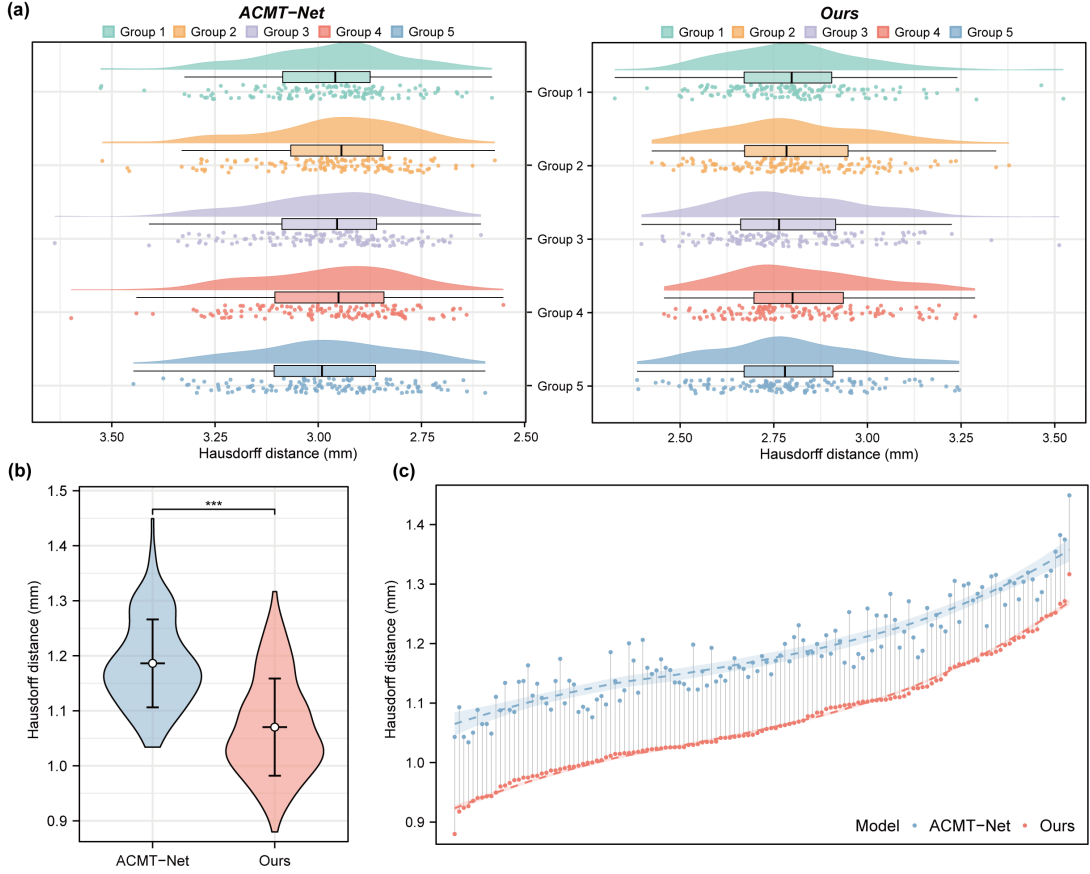


**Figure 5. Comparison of point cloud error between ACMT-Net and our proposed model.** (a) Hausdorff distance for five groups of sparse point sets, comparing ACMT-Net (left) and our model (right). (b) Prediction error on dense point sets, showing a significant reduction in Hausdorff distance with our model. (c) Case-wise paired comparison of point cloud error for individual cases.

**Fig.6** presents a qualitative comparison of 3D surface meshes reconstructed from predicted point clouds and corresponding ground truth. The error distributions are visualized in the heatmaps shown in **Fig.7a**. Quantitative analysis revealed that the surface deviation error of PhysSFI-Net ( $1.296 \pm 0.349$  mm) was significantly lower than that of ACMT-Net ( $1.372 \pm 0.351$  mm) (**Fig.7b–c**), further confirming the enhanced accuracy of our method. To assess anatomical fidelity, we evaluated the prediction accuracy across 15 clinically significant craniofacial landmarks, including five periorbital, four midfacial, and six perioral/chin landmarks (**Fig.8a**; **Table S3**). As shown in **Fig.8b**, the overall landmark error for PhysSFI-Net was  $2.445 \pm 1.326$  mm, significantly lower than that of ACMT-Net ( $2.930 \pm 1.555$  mm). At the individual landmark level, PhysSFI-Net consistently outperformed ACMT-Net, with statistically significant improvements observed at key landmarks including sICaL, sOCaR, sPrn, sSn, sAIL, sAIR, sChU, sChL, sChR, sPog, and sMe (**Fig.8c**). Given that a landmark error of less than 2 mm is generally regarded as clinically acceptable, we further examined the distribution of landmark errors using 2 mm and 4 mm as thresholds. PhysSFI-Net yielded a significantly higher proportion of landmarks with errors below 2 mm and a lower proportion exceeding 4 mm when compared to ACMT-Net (**Fig.8d**), demonstrating its superior

clinical relevance and robustness.

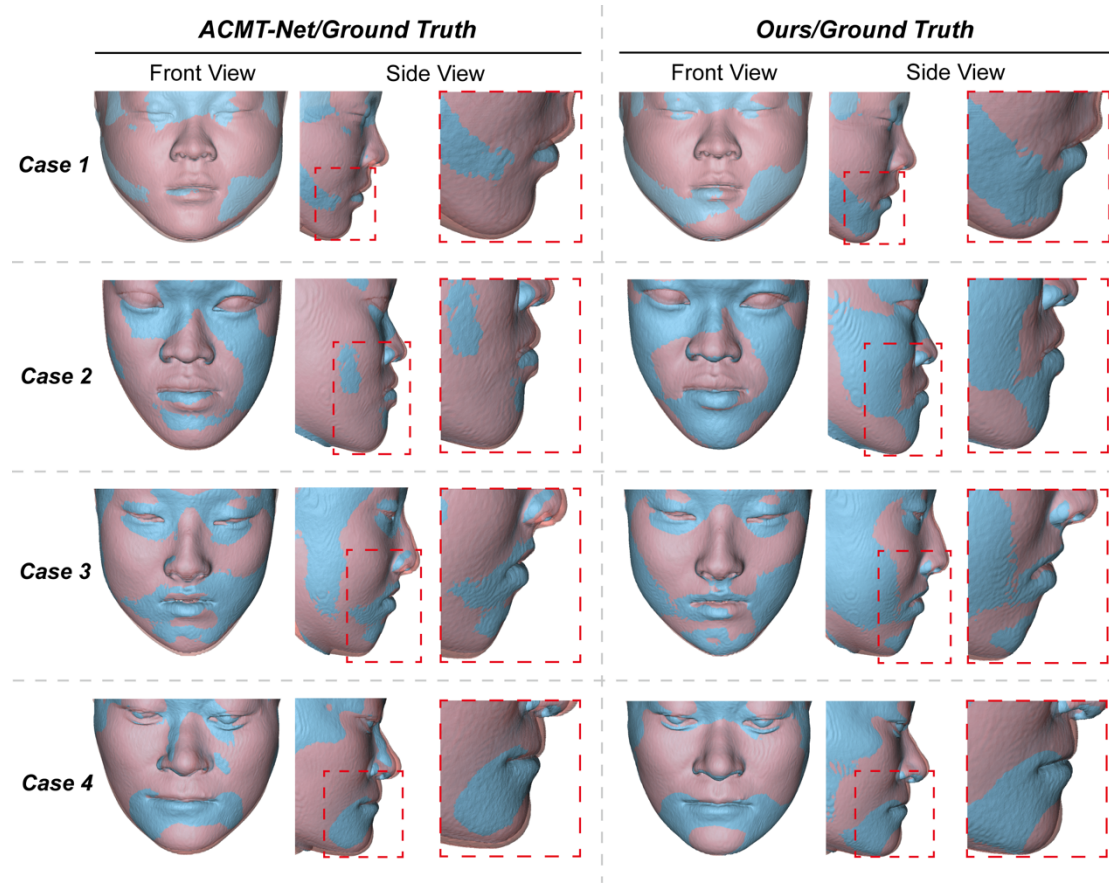


**Figure 6. Qualitative comparison of postoperative facial appearance prediction between ACMT-Net and our model.** Four representative cases are shown with front and side views. Red surfaces represent the ground truth, and blue surfaces represent the predicted results.

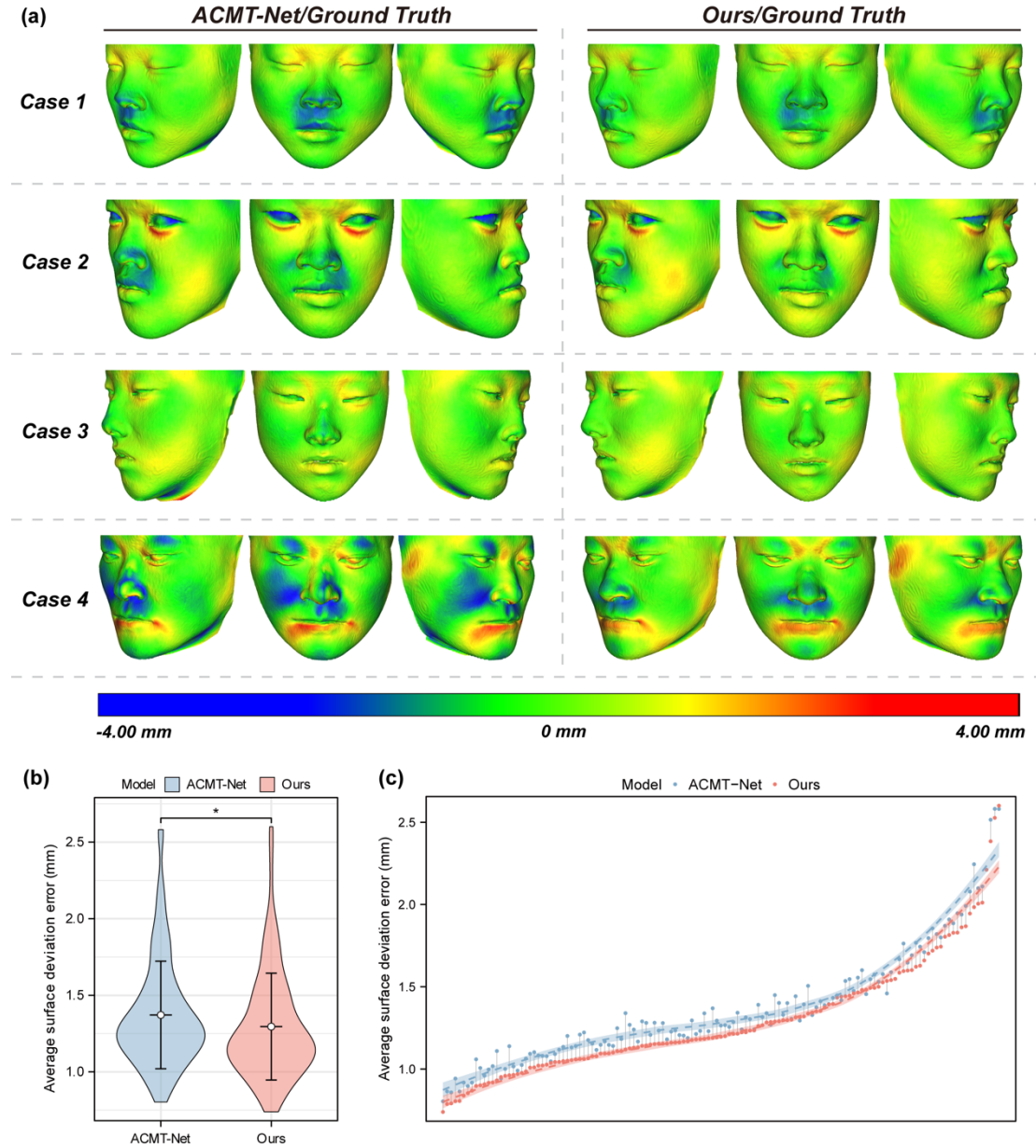


**Figure 7. Quantitative evaluation of surface deviation errors between ACMT-Net and the proposed model.** (a) Heatmap visualizations of surface deviation errors for four representative cases. The color scale indicates deviation magnitude from  $-4.00$  mm (blue) to  $+4.00$  mm (red), with green representing minimal error. (b) Violin plots of average surface deviation error shows that our model achieves significantly lower errors than ACMT-Net ( $*p < 0.05$ ). (c) Case-wise paired comparison of average surface deviation error, with most samples showing reduced error using our method.

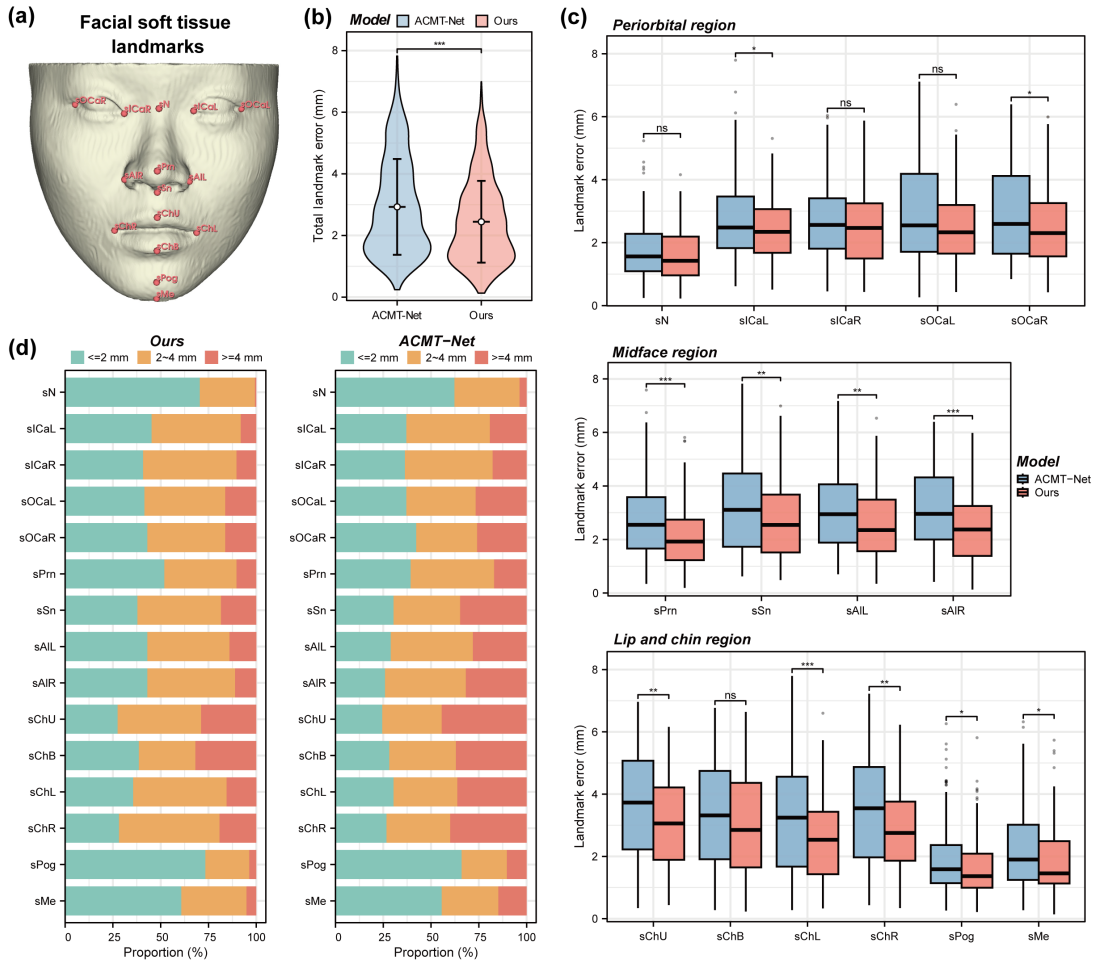


**Figure 8. Landmark-based evaluation of soft-tissue prediction accuracy.** (a) Definition of 19 facial soft-tissue landmarks used for accuracy evaluation. (b) Violin plots showing total landmark error across all points, with our model demonstrating significantly lower errors than ACMT-Net (\*\*p < 0.001). (c) Landmark error comparison across periorbital, midface, and lip/chin regions. (d) Proportion of predicted landmarks within three error ranges (<2 mm, 2–4 mm, and >4 mm), illustrating the overall improvement in accuracy with our model.

## 4. Discussion

Prediction of postoperative facial appearance is critical for optimizing orthognathic surgical plan. Conventional approaches integrated into existing clinical software often suffer from limited predictive precision. The development of fast and accurate prediction methods remains an unmet need. In this study, we propose a physics-informed geometric deep learning framework, named PhysSFI-Net. We designed a hierarchical graph representation method to encode the geometric and topological relationships among facial soft tissues, skeletal anatomy, and planned surgical movements. It incorporates an attention mechanism to estimate the postoperative facial displacement field and integrates an LSTM-based soft-tissue deformation module to capture the temporally continuous and biomechanically driven nature of soft tissue response. Comprehensive evaluations using multiple quantitative metrics confirm its superior performance relative to existing

state-of-the-art approaches.

Biomechanical simulations (e.g., finite element modeling) can produce realistic results but often struggle to balance accuracy and speed, making routine clinical use difficult(D. Kim et al., 2017, 2021). To overcome these limitations, researchers have turned to geometry-based deep learning frameworks that learn the mapping from skeletal movements to soft-tissue deformation directly from patient data. Notable examples include FSC-Net, DGCFP and ACMT-Net, which leverage neural networks to extract bone displacement features and infer soft-tissue deformations(Fang et al., 2024; Huang et al., 2025; Ma et al., 2023). For instance, Huang et al, proposed DGCFP for postoperative facial prediction, which consist of multi-scale dualconv face encoder, pointwise bone encoder, dual-space movement transfer and coarse-to-fine deformation(Huang et al., 2025). ACMT-Net introduced an attentive bone–soft-tissue correspondence mechanism to achieve FEM-level accuracy with significantly improved efficiency(Fang et al., 2024). Our proposed PhysSFI-Net offers the dual benefit of speed and precision, which produces 3D facial surface predictions within seconds, with a dense point cloud error of  $1.070 \pm 0.088$  mm and mesh reconstruction error of  $1.296 \pm 0.349$  mm.

The motivation for incorporating an LSTM module in PhysSFI-Net arises from the recognition that facial soft-tissue deformation is fundamentally biomechanical and involves incremental changes under mechanical forces(Lampen et al., 2024). Purely geometric approaches typically model static shape correspondences, potentially overlooking the dynamic and cumulative nature of soft-tissue deformation driven by biomechanical interactions. Previous studies have attempted to integrate physical principles into deep learning frameworks to improve model interpretability by incorporating physics-informed constraints. Lampen et al. introduced a biomechanics-informed deep neural network based on the PointNet++ and subsequently proposed a DL method named Spatiotemporal Incremental Mechanics Modeling based on PhysGNN, to perform spatiotemporal incremental simulations of soft tissue mechanical modeling(Lampen et al., 2024). LSTM is a type of recurrent neural network designed to effectively model sequential data and capture long-range dependencies(Feng et al., 2023; Vennerød et al., 2021). Karami et al. combined CNN and LSTM layers with a mass-conservation loss to simulate viscoelastic tissue behavior(Karami et al., 2023). Likewise, Nguyen-Le et al. employed an LSTM-based network to predict pelvic soft-tissue deformation in childbirth simulation(Nguyen-Le et al., 2023). These approaches show that LSTM can capture nonlinear, time-dependent mechanical behavior by learning how deformations evolve in sequence. Building on this concept, PhysSFI-Net incorporates an LSTM-based incremental deformation module, enabling the network to simulate soft-tissue deformation through a sequence of cumulative steps driven by mechanical forces. This stepwise approach significantly improves the model’s interpretability, as each incremental LSTM step represents an intermediate stage of deformation, thereby ensuring biomechanical plausibility and reducing physically unrealistic distortions.

Within the broader landscape of prediction approaches in orthognathic surgery planning, 3D soft-tissue outcome modeling is widely acknowledged as one of the most difficult aspects.

Numerous recent approaches have been developed to address this challenge from diverse methodological perspectives. Kim et al. introduced a graph learning-based prediction method using lateral cephalograms, named Dual Embedding Module Graph Convolutional Neural Network, which was developed to predict the displacement of key skeletal landmarks such as ANS, PNS, B-point and Md1crown(I.-H. Kim et al., 2023). Building on that, they recently developed GPOSNet, a generative approach that first predicts postoperative landmark shifts with a graph neural network and then synthesizes a realistic postoperative lateral cephalogram using a latent diffusion model(I.-H. Kim et al., 2025). Other researchers have focused on parametric modeling of the face. Qiu et al. developed SCULPTOR, a skeleton-consistent face generator that jointly models the skull and facial surface in a unified data-driven framework, which can produce anatomically plausible facial modifications and simulate surgical outcomes(Qiu et al., 2022). In addition, Han et al. proposed an automated pipeline based on the FLAME 3D morphable model to predict postoperative facial appearance, reporting mean errors of approximately 9 mm in Hausdorff distance and 2.5 mm in Chamfer distance(Olivetti et al., 2025). Compared to these methods, PhysSFI-Net directly predicts the complete 3D soft-tissue morphology rather than being limited to cephalometric projections, resulting in predictions closer to actual postoperative outcomes. Its physics-informed LSTM architecture enhances interpretability and biomechanical realism, addressing limitations inherent in purely statistical or generative approaches. These features collectively position PhysSFI-Net as a comprehensive and clinically relevant approach for orthognathic surgical outcome simulation.

The other major strengths of this study lie in the sample size of the dataset used for model training and validation. Previous studies often relied on small 3D datasets, typically comprising approximately 40 paired samples, which restrict the generalizability and stability of predictive models. Some studies have utilized synthetic data generated from finite element simulations(Lampen et al., 2022, 2024). While such data incorporate biomechanical assumptions, they do not reflect the anatomical variability present in real clinical cases. To overcome these limitations, we constructed the largest dataset to date containing paired preoperative and postoperative 3D facial and skeletal models from real orthognathic surgery patients. This dataset includes a wide spectrum of skeletal deformities and surgical plans, providing strong representativeness, diversity, and anatomical completeness. Furthermore, we applied a five-fold cross-validation approach to rigorously assess model performance across different subsets of the data. This strategy enhances the robustness and generalizability of the proposed PhysSFI-Net framework and supports its potential for clinical application.

Our study has several limitations. First, the dataset was derived from a single center, potentially limiting its generalizability to broader patient populations. Soft-tissue reconstructions generated from CT data lack critical color and texture information. Second, our current prediction framework does not adequately incorporate patient-specific characteristics, and several preprocessing steps still rely on manual intervention. Achieving a fully automated, end-to-end predictive pipeline remains a significant objective to enhance clinical applicability. Third, accurately predicting soft-tissue deformation in anatomically complex regions, particularly around the lips, remains a significant

challenge. Factors such as surgical suture techniques, intraoral orthodontic brackets and patient movements during CT imaging can substantially influence prediction accuracy. Developing standardized methods to systematically extract and represent individual soft-tissue features in these complex anatomical regions is essential for improving model robustness and precision.

## 5. Conclusion

In this study, we proposed PhysSFI-Net, a physics-informed deep learning framework that integrates hierarchical graph representations, attention-based feature encoding, and an LSTM-driven soft-tissue deformation module to simulate biomechanically realistic facial changes. Our model demonstrated high prediction accuracy across multiple quantitative metrics and outperformed the current state-of-the-art method, highlighting its potential value in advancing personalized orthognathic surgical planning and decision support in clinical practice.

## 6. Data Statements

The de-identified data and source code used and/or analyzed during the current study are available from the corresponding author upon reasonable request.

## 7. Declaration of competing interests

The authors declare that they have no known competing financial interests or personal relationships that could have appeared to influence the work reported in this paper.

## 8. Reference

- Bao, J., Tan, Z., Sun, Y., Xu, X., Liu, H., Cui, W., Yang, Y., Cheng, M., Wang, Y., Ku, C., Ho, Y. K., Zhu, J., Fan, L., Qian, D., Shen, S., Wen, Y., & Yu, H. (2025). Deep ensemble learning-driven fully automated multi-structure segmentation for precision craniomaxillofacial surgery. *Frontiers in Bioengineering and Biotechnology*, 13, 1580502. <https://doi.org/10.3389/fbioe.2025.1580502>
- Bao, J., Zhang, X., Xiang, S., Liu, H., Cheng, M., Yang, Y., Huang, X., Xiang, W., Cui, W., Lai, H. C., Huang, S., Wang, Y., Qian, D., & Yu, H. (2024). Deep Learning-Based Facial and Skeletal Transformations for Surgical Planning. *Journal of Dental Research*, 220345241253186. <https://doi.org/10.1177/00220345241253186>
- Chabanas, M., Luboz, V., & Payan, Y. (2003). Patient specific finite element model of the face soft tissues for computer-assisted maxillofacial surgery. *Medical Image Analysis*, 7(2), 131–151. [https://doi.org/10.1016/s1361-8415\(02\)00108-1](https://doi.org/10.1016/s1361-8415(02)00108-1)
- Chagnon, G., Rebouah, M., & Favier, D. (2015). Hyperelastic Energy Densities for Soft Biological Tissues: A Review. *Journal of Elasticity*, 120(2), 129–160. <https://doi.org/10.1007/s10659-014-9508-z>
- Cheng, M., Zhuang, Y., Zhao, H., Li, M., Fan, L., & Yu, H. (2022). Development of a maxillofacial virtual surgical system based on biomechanical parameters of facial soft tissue. *International Journal of Computer Assisted Radiology and Surgery*, 17(7), 1201–1211. <https://doi.org/10.1007/s11548-022-02657-5>
- Cho, S. J., Moon, J.-H., Ko, D.-Y., Lee, J.-M., Park, J.-A., Donatelli, R. E., & Lee, S.-J. (2024). Orthodontic treatment outcome predictive performance differences between artificial intelligence and conventional methods. *The Angle Orthodontist*, 94(5), 557–565. <https://doi.org/10.2319/111823-767.1>
- Dunworth, K., Hernandez, J. A., Ching, J., Golden, B., Nguyen, P. D., Patel, K., Rogers-Vizena, C. R., Rottgers, S. A., & Allori, A. C. (2024). Aesthetic Outcomes in Cleft Care: Exploring Patterns in Patient-Reported Outcomes across Adolescence. *Plastic and Reconstructive Surgery*, 154(4), 841.

<https://doi.org/10.1097/PRS.00000000000011098>

- Fang, X., Kim, D., Xu, X., Kuang, T., Deng, H. H., Barber, J. C., Lampen, N., Gateno, J., Liebschner, M. A. K., Xia, J. J., & Yan, P. (2022). Deep Learning-Based Facial Appearance Simulation Driven by Surgically Planned Craniomaxillofacial Bony Movement. In L. Wang, Q. Dou, P. T. Fletcher, S. Speidel, & S. Li (Eds.), *Medical Image Computing and Computer Assisted Intervention – MICCAI 2022* (pp. 565–574). Springer Nature Switzerland. [https://doi.org/10.1007/978-3-031-16449-1\\_54](https://doi.org/10.1007/978-3-031-16449-1_54)
- Fang, X., Kim, D., Xu, X., Kuang, T., Lampen, N., Lee, J., Deng, H. H., Liebschner, M. A. K., Xia, J. J., Gateno, J., & Yan, P. (2024). Correspondence attention for facial appearance simulation. *Medical Image Analysis*, 93, 103094. <https://doi.org/10.1016/j.media.2024.103094>
- Feng, W., Zhang, W., Meng, M., Gong, Y., & Gu, F. (2023). A Novel Binary Classification Algorithm for Carpal Tunnel Syndrome Detection Using LSTM. *2023 IEEE 3rd International Conference on Software Engineering and Artificial Intelligence (SEAI)*, 143–147. <https://doi.org/10.1109/SEAI59139.2023.10217512>
- Hertanto, M., Ayoub, A. F., Benington, P. C. M., Naudi, K. B., & McKenzie, P. S. (2021). Orthognathic patient perception of 3D facial soft tissue prediction planning. *Journal of Cranio-Maxillo-Facial Surgery: Official Publication of the European Association for Cranio-Maxillo-Facial Surgery*, 49(9), 783–788. <https://doi.org/10.1016/j.jcms.2021.03.009>
- Ho, C.-T., Lin, H.-H., & Lo, L.-J. (2019). Intraoral Scanning and Setting Up the Digital Final Occlusion in Three-Dimensional Planning of Orthognathic Surgery: Its Comparison with the Dental Model Approach. *Plastic and Reconstructive Surgery*, 143(5), 1027e. <https://doi.org/10.1097/PRS.0000000000005556>
- Hsu, S. S.-P., Gateno, J., Bell, R. B., Hirsch, D. L., Markiewicz, M. R., Teichgraeber, J. F., Zhou, X., & Xia, J. J. (2013). Accuracy of a computer-aided surgical simulation protocol for orthognathic surgery: A prospective multicenter study. *Journal of Oral and Maxillofacial Surgery: Official Journal of the American Association of Oral and Maxillofacial Surgeons*, 71(1), 128–142. <https://doi.org/10.1016/j.joms.2012.03.027>
- Huang, X., He, D., Li, Z., Zhang, X., & Wang, X. (2025). Maxillofacial bone movements-aware dual graph convolution approach for postoperative facial appearance prediction. *Medical Image Analysis*, 99, 103350. <https://doi.org/10.1016/j.media.2024.103350>
- Karami, M., Lombaert, H., & Rivest-Hénault, D. (2023). Real-time simulation of viscoelastic tissue behavior with physics-guided deep learning. *Computerized Medical Imaging and Graphics*, 104, 102165. <https://doi.org/10.1016/j.compmedimag.2022.102165>
- Khalid, M. A., Khurshid, A., Zulfiqar, K., Bashir, U., & Fraz, M. M. (2024). A two-stage regression framework for automated cephalometric landmark detection incorporating semantically fused anatomical features and multi-head refinement loss. *Expert Systems with Applications*, 255, 124840. <https://doi.org/10.1016/j.eswa.2024.124840>
- Kim, D., Ho, D. C., Mai, H., Zhang, X., Shen, S. G. F., Shen, S., Yuan, P., Liu, S., Zhang, G., Zhou, X., Gateno, J., Liebschner, M. A. K., & Xia, J. J. (2017). A clinically validated prediction method for facial soft-tissue changes following double-jaw surgery. *Medical Physics*, 44(8), 4252–4261. <https://doi.org/10.1002/mp.12391>
- Kim, D., Kuang, T., Rodrigues, Y. L., Gateno, J., Shen, S. G. F., Wang, X., Stein, K., Deng, H. H., Liebschner, M. A. K., & Xia, J. J. (2021). A novel incremental simulation of facial changes following orthognathic surgery using FEM with realistic lip sliding effect. *Medical Image Analysis*, 72, 102095. <https://doi.org/10.1016/j.media.2021.102095>
- Kim, I.-H., Jeong, J., Kim, J.-S., Lim, J., Cho, J.-H., Hong, M., Kang, K.-H., Kim, M., Kim, S.-J., Kim, Y.-J., Sung, K., & Lee, J. (2023). A deep learning framework for facial soft-tissue prediction following orthognathic surgery. *Journal of Cranio-Maxillo-Facial Surgery: Official Publication of the European Association for Cranio-Maxillo-Facial Surgery*, 51(10), 1831–1838. <https://doi.org/10.1016/j.jcms.2023.102095>

- S.-J., Kim, Y. H., Lim, S.-H., Baek, S.-H., Park, J.-W., & Kim, N. (2025). Predicting orthognathic surgery results as postoperative lateral cephalograms using graph neural networks and diffusion models. *Nature Communications*, 16(1), 2586. <https://doi.org/10.1038/s41467-025-57669-x>
- Kim, I.-H., Kim, J.-S., Jeong, J., Park, J.-W., Park, K., Cho, J.-H., Hong, M., Kang, K.-H., Kim, M., Kim, S.-J., Kim, Y.-J., Sung, S.-J., Kim, Y. H., Lim, S.-H., Baek, S.-H., & Kim, N. (2023). Orthognathic surgical planning using graph CNN with dual embedding module: External validations with multi-hospital datasets. *Computer Methods and Programs in Biomedicine*, 242, 107853. <https://doi.org/10.1016/j.cmpb.2023.107853>
- Lampen, N., Kim, D., Fang, X., Xu, X., Kuang, T., Deng, H. H., Barber, J. C., Gateno, J., Xia, J., & Yan, P. (2022). Deep learning for biomechanical modeling of facial tissue deformation in orthognathic surgical planning. *International Journal of Computer Assisted Radiology and Surgery*, 17(5), 945–952. <https://doi.org/10.1007/s11548-022-02596-1>
- Lampen, N., Kim, D., Xu, X., Fang, X., Lee, J., Kuang, T., Deng, H. H., Liebschner, M. A. K., Gateno, J., & Yan, P. (2024). Learning soft tissue deformation from incremental simulations. *Medical Physics*. <https://doi.org/10.1002/mp.17554>
- Liang, S., Lu, X., Ren, S., Chen, T., Ma, J., He, C., Shi, Z., & Gu, F. (2026). A novel obstructive sleep apnea detection model based on multi-scale convolutional neural networks. *Expert Systems with Applications*, 299, 130312. <https://doi.org/10.1016/j.eswa.2025.130312>
- Lin, G., Yang, S., Chen, Y., Xu, Q., Yap, P.-T., Yun, Z., & Feng, Q. (2025). TransFArchNet: Predicting dental arch curves based on facial point clouds in personalized panoramic X-ray imaging. *Expert Systems with Applications*, 270, 126577. <https://doi.org/10.1016/j.eswa.2025.126577>
- Ma, L., Xiao, D., Kim, D., Lian, C., Kuang, T., Liu, Q., Deng, H., Yang, E., Liebschner, M. A. K., Gateno, J., Xia, J., & Yap, P.-T. (2023). Simulation of Postoperative Facial Appearances via Geometric Deep Learning for Efficient Orthognathic Surgical Planning. *IEEE Transactions on Medical Imaging*, 42(2), 336–345. *IEEE Transactions on Medical Imaging*. <https://doi.org/10.1109/TMI.2022.3180078>
- Mollemans, W., Schutyser, F., Nadjmi, N., Maes, F., & Suetens, P. (2007). Predicting soft tissue deformations for a maxillofacial surgery planning system: From computational strategies to a complete clinical validation. *Medical Image Analysis*, 11(3), 282–301. <https://doi.org/10.1016/j.media.2007.02.003>
- Naran, S., Steinbacher, D. M., & Taylor, J. A. (2018). Current Concepts in Orthognathic Surgery. *Plastic and Reconstructive Surgery*, 141(6), 925e–936e. <https://doi.org/10.1097/PRS.0000000000004438>
- Nguyen-Le, D. H., Ballit, A., & Dao, T.-T. (2023). A novel deep learning-driven approach for predicting the pelvis soft-tissue deformations toward a real-time interactive childbirth simulation. *Engineering Applications of Artificial Intelligence*, 126, 107150. <https://doi.org/10.1016/j.engappai.2023.107150>
- Olivetti, E. C., Marcolin, F., Moos, S., Vezzetti, E., Borbon, C., Zavattero, E., & Ramieri, G. (2025). How to predict the future face? A 3D methodology to forecast the aspect of patients after orthognathic surgeries. *Computer Methods and Programs in Biomedicine*, 265, 108757. <https://doi.org/10.1016/j.cmpb.2025.108757>
- Pellitteri, F., Albertini, P., Bruculeri, L., Cremonini, F., Guiducci, D., Falconi, V., & Lombardo, L. (2025). Soft tissue changes during orthopedic therapy: An in vivo 3-dimensional facial scan study. *American Journal of Orthodontics and Dentofacial Orthopedics*, 167(2), 154–165. <https://doi.org/10.1016/j.ajodo.2024.08.016>
- Qiu, Z., Li, Y., He, D., Zhang, Q., Zhang, L., Zhang, Y., Wang, J., Xu, L., Wang, X., Zhang, Y., & Yu, J. (2022). SCULPTOR: Skeleton-Consistent Face Creation Using a Learned Parametric Generator. *ACM Transactions on Graphics*, 41(6), 213:1–213:17. <https://doi.org/10.1145/3550454.3555462>
- Ruggiero, F., Badiali, G., Bevini, M., Marchetti, C., Ong, J., Bolognesi, F., Schievano, S., Dunaway, D., Bianchi, A.,

- & Borghi, A. (2022). Parametrizing the genioplasty: A biomechanical virtual study on soft tissue behavior. *International Journal of Computer Assisted Radiology and Surgery*, 17(1), 55–64. <https://doi.org/10.1007/s11548-021-02489-9>
- Ruggiero, F., Borghi, A., Bevini, M., Badiali, G., Lunari, O., Dunaway, D., & Marchetti, C. (2023). Soft tissue prediction in orthognathic surgery: Improving accuracy by means of anatomical details. *PloS One*, 18(11), e0294640. <https://doi.org/10.1371/journal.pone.0294640>
- Singer, A. (2006). From graph to manifold Laplacian: The convergence rate. *Applied and Computational Harmonic Analysis*, 21(1), 128–134. <https://doi.org/10.1016/j.acha.2006.03.004>
- Vennerød, C. B., Kjærren, A., & Bugge, E. S. (2021). *Long Short-term Memory RNN* (No. arXiv:2105.06756). arXiv. <https://doi.org/10.48550/arXiv.2105.06756>
- Wang, Y., Li, X., Yang, Y., Cheng, M., Zhang, X., Bao, J., Qian, H., Huang, X., Wu, Z., Xiang, S., Wen, Y., & Yu, H. (2025). Ortho-OPD: An Automatic Osteotomy Planes Design Model for Orthognathic Surgery Based on Deep Learning. *IEEE Journal of Biomedical and Health Informatics*, 1–14. <https://doi.org/10.1109/JBHI.2025.3638775>
- Xia, J. J., Gateno, J., Teichgraeber, J. F., Yuan, P., Li, J., Chen, K.-C., Jajoo, A., Nicol, M., & Alfi, D. M. (2015). Algorithm for planning a double-jaw orthognathic surgery using a computer-aided surgical simulation (CASS) protocol. Part 2: Three-dimensional cephalometry. *International Journal of Oral and Maxillofacial Surgery*, 44(12), 1441–1450. <https://doi.org/10.1016/j.ijom.2015.06.007>
- Xie, D., Duan, X., Fang, F., Ma, L., Zhao, M., Lu, J., & Li, C. (2026). Mixed reality versatile platform for intraoperative navigation of craniomaxillofacial plastic surgery. *Expert Systems with Applications*, 299, 130106. <https://doi.org/10.1016/j.eswa.2025.130106>
- Xing, K., Mei, H., Feng, Q., Quan, S., Zhang, G., Jia, A., Ge, H., Mei, D., & Li, J. (2023). Accuracy in predicting soft tissue changes of orthodontic class III cases using Dolphin® software. *Clinical Oral Investigations*, 27(8), 4531–4539. <https://doi.org/10.1007/s00784-023-05077-0>
- Zhang, J., Ye, Z., Chen, M., Yu, J., & Cheng, Y. (2025). TransGraphNet: A novel network for medical image segmentation based on transformer and graph convolution. *Biomedical Signal Processing and Control*, 104, 107510. <https://doi.org/10.1016/j.bspc.2025.107510>
- Zhang, R., Jie, B., He, Y., & Wang, J. (2025). TCFNet: Bidirectional face-bone transformation via a Transformer-based coarse-to-fine point movement network. *Medical Image Analysis*, 105, 103653. <https://doi.org/10.1016/j.media.2025.103653>
- Zheng, M., Yang, X., Li, X., Luo, X., Liu, X., Tang, K., Meng, H., & Shen, L. (2026). Text condition embedded regression network for automated dental implant abutment design. *Expert Systems with Applications*, 299, 130160. <https://doi.org/10.1016/j.eswa.2025.130160>

## 9. Figure Legends

**Figure 1. The overview of the study pipeline.** (a) Patient selection and data acquisition. (b) Data annotation. (c) Point cloud sampling. (d) Model design. (e) Training and evaluation.

**Figure 2. The detailed architecture of Physics-Informed Skeletal-Facial Interaction Network (PhysSFI-Net).** (a) Image segmentation and point cloud sampling. (b) A hierarchical feature extraction approach, consisting of a craniofacial correspondence feature encoder and a surgical plan feature encoder, combined with an attention mechanism designed to predict facial displacement features. (c) A sequential prediction approach that employs three LSTM modules to simulate incremental soft tissue deformation guided by mechanical states. (d) An electromechanics-inspired high-precision reconstruction method, facilitating accurate 3D reconstruction of postoperative facial morphology.

**Figure 3.** Training and validation logs of PhysSFI-Net under different numbers of LSTM layers.

**Figure 4. Summary of patient characteristics and surgical procedures.** (a) Clinical features of 135 patients, including age, gender, BMI, skeletal discrepancy, facial asymmetry, and vertical facial type. (b) Types of orthognathic procedures performed, including Le Fort I osteotomy, BSSRO, genioplasty, and paranasal bone grafting. (c) Distribution of surgical combinations across the dataset shown using an Upset plot. (d) Example of virtual surgical planning workflow.

**Figure 5. Comparison of point cloud error between ACMT-Net and our proposed model.** (a) Hausdorff distance for five groups of sparse point sets, comparing ACMT-Net (left) and our model (right). (b) Prediction error on dense point sets, showing a significant reduction in Hausdorff distance with our model. (c) Case-wise paired comparison of point cloud error for individual cases.

**Figure 6. Qualitative comparison of postoperative facial appearance prediction between ACMT-Net and our model.** Four representative cases are shown with front and side views. Red surfaces represent the ground truth, and blue surfaces represent the predicted results.

**Figure 7. Quantitative evaluation of surface deviation errors between ACMT-Net and the proposed model.** (a) Heatmap visualizations of surface deviation errors for four representative cases. The color scale indicates deviation magnitude from  $-4.00$  mm (blue) to  $+4.00$  mm (red), with green representing minimal error. (b) Violin plots of average surface deviation error shows that our model achieves significantly lower errors than ACMT-Net ( $*p < 0.05$ ). (c) Case-wise paired comparison of average surface deviation error, with most samples showing reduced error using our method.

**Figure 8. Landmark-based evaluation of soft-tissue prediction accuracy.** (a) Definition of 19 facial soft-tissue landmarks used for accuracy evaluation. (b) Violin plots showing total landmark error across all points, with our model demonstrating significantly lower errors than ACMT-Net ( $***p < 0.001$ ). (c) Landmark error comparison across periorbital, midface, and lip/chin regions. (d) Proportion of predicted landmarks within three error ranges ( $<2$  mm,  $2-4$  mm, and  $>4$  mm), illustrating the overall improvement in accuracy with our model.

## Supplemental Appendix

### PhysSFI-Net: Physics-informed Geometric Learning of Skeletal and Facial Interactions for Orthognathic Surgical Outcome Prediction

Jiahao Bao<sup>1#</sup>, Huazhen Liu<sup>2#</sup>, Yu Zhuang<sup>3#</sup>, Lieran Tao<sup>4</sup>, Xinyu Xu<sup>5</sup>, Yongtao Shi<sup>6</sup>, Mengjia Cheng<sup>7</sup>, Yiming Wang<sup>8</sup>, Congshuang Ku<sup>9</sup>, Ting Zeng<sup>10</sup>, Yilang Du<sup>11</sup>, Siyi Chen<sup>12</sup>, Shunyao Shen<sup>13\*</sup>, Suncheng Xiang<sup>14\*</sup>, Hongbo Yu<sup>15\*</sup>

#### Supplemental Figures:

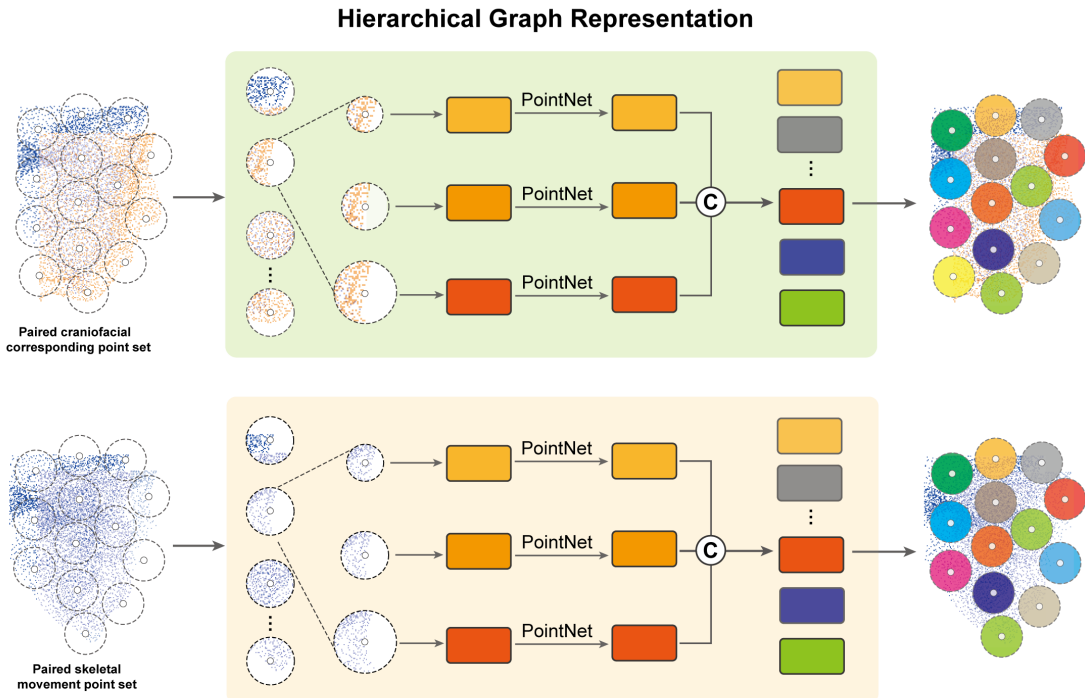


**Figure S1.** The detailed architecture of hierarchical graph representation module in Physics-Informed Skeletal-Facial Interaction Network (PhysSFI-Net).

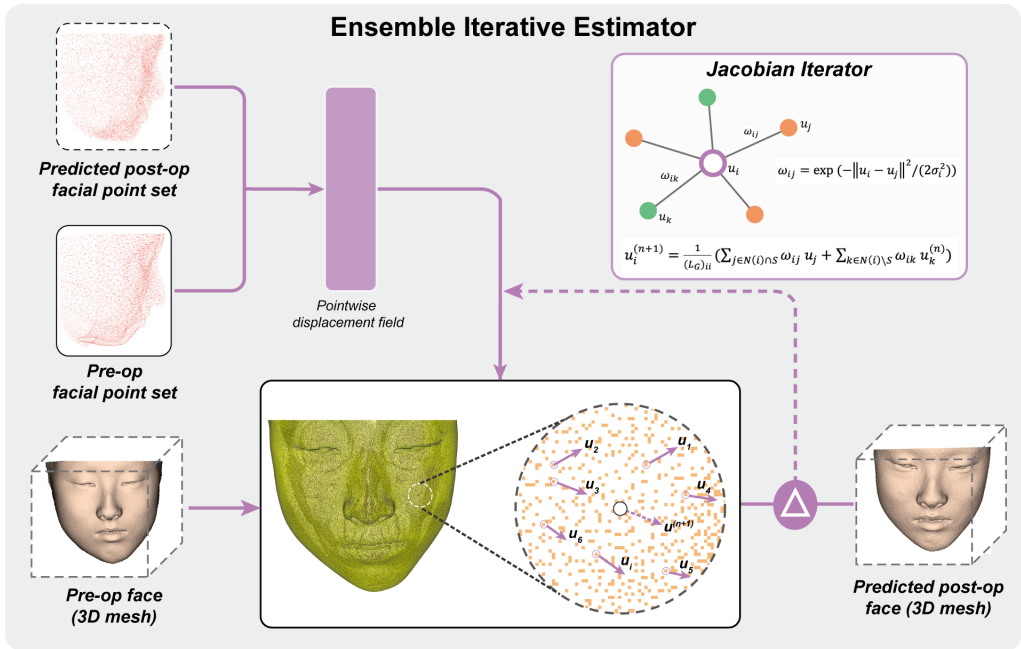


**Figure S2.** The detailed architecture of ensemble iterative estimator in Physics-Informed Skeletal-Facial Interaction Network (PhysSFI-Net)

**Supplemental Tables:**

**Table S1. Characteristics of study participants**

characteristics	Overall
n	135
<b>Gender, n (%)</b>	
Female	92 (68.1%)
Male	43 (31.9%)
<b>Age, median (IQR)</b>	
	22 (20, 25)
<b>BMI, n (%)</b>	
<18.5	14 (10.4%)
18.5~25	104 (77%)
>25	17 (12.6%)
<b>Skeletal Discrepancy, n (%)</b>	
<b>Clinical feature</b>	
Class I ( $0 \leq \text{ANB} < 4$ )	12 (8.9%)
Class II ( $4 \leq \text{ANB}$ )	24 (17.8%)
Class III ( $\text{ANB} < 0$ )	99 (73.3%)
<b>Facial Asymmetry, n (%)</b>	
Without	52 (38.5%)
With	83 (61.5%)
<b>FH-MP, n (%)</b>	
Average-angle	50 (37%)
High-angle	76 (56.3%)
Low-angle	9 (6.7%)
<b>LeFort I, n (%)</b>	
Y	121 (89.6%)
N	14 (10.4%)
<b>Surgery Type</b>	
<b>BSSRO, n (%)</b>	
Y	132 (97.8%)
N	3 (2.2%)

<b>Genioplasty, n (%)</b>			
	Y		23 (17%)
	N		112 (83%)
<b>PBG (L), n (%)</b>			
	Y		32 (23.7%)
	N		103 (76.3%)
<b>PBG (R), n (%)</b>			
	Y		29 (21.5%)
	N		106 (78.5%)

**Table S2. Hausdorff distance for five groups of sparse point sets predicted by ACMT-Net and our model.**

	ACMT-Net		Ours	
	mean	sd	mean	sd
Group 1	2.982	0.176	2.804	0.194
Group 2	2.968	0.179	2.809	0.196
Group 3	2.979	0.178	2.803	0.194
Group 4	2.976	0.182	2.819	0.186
Group 5	2.985	0.176	2.788	0.187
Dense	1.186	0.080	1.070	0.088

**Table S3. Definition of CMF landmarks.**

Region	Landmark	Definition	
Periorbital region	sN	Soft Tissue Nasion	Medial (and upper) point of the nasal root

	sICaL	Inner Canthus Left	The soft tissue point located at the inner commissure of the left eye fissure
	sICaR	Inner Canthus Right	The soft tissue point located at the inner commissure of the right eye fissure
	sOCaL	Outer Canthus Left	The soft tissue point located at the inner commissure of the left eye fissure
	sOCaR	Outer Canthus Right	The soft tissue point located at the outer commissure of the right eye fissure
<b>Midface</b> <b>region</b>	sPrn	Pronasale	Most prominent point on nasal tip
	sSn	Subnasale	Junction between columella and upper lip
	sAlL	Alare Left	The most lateral point on the left alar contour
	sAlR	Alare Right	The most lateral point on the right alar contour
<b>Lip and chin</b> <b>region</b>	sChU	Cheilion Upper	The midpoint of the vermillion line of the upper lip
	sChB	Cheilion Lower	The midpoint of the vermillion line of the lower lip
	sChL	Cheilion Left	The point located at the left labial commissure
	sChR	Cheilion Right	The point located at the right labial commissure
<b>Chin</b> <b>region</b>	sPog	Soft tissue Pogonion	Medial and most anterior point of the chin
	sMe	Soft tissue Menton	Medial and lowest point of the chin